

ORIGINAL ARTICLE

Multipath optical thermometry realized in $\text{CaSc}_2\text{O}_4: \text{Yb}^{3+}/\text{Er}^{3+}$ with high sensitivity and superior resolution

Guotao Xiang¹  | Qing Xia¹ | Su Xu¹ | Xiuchong Liu¹ | Sha Jiang¹  | Yongjie Wang¹ | Xianju Zhou¹  | Li Li¹  | Li Ma³ | Xiaojun Wang³ | Jiahua Zhang²

¹Department of Mathematics and Physics, Chongqing University of Posts and Telecommunications, Chongqing, China

²State Key Laboratory of Luminescence and Applications, Changchun Institute of Optics, Fine Mechanics and Physics, Chinese Academy of Sciences, Changchun, China

³Department of Physics & Astronomy, Georgia Southern University, Statesboro, GA, USA

Correspondence

Guotao Xiang, Department of Mathematics and Physics, Chongqing University of Posts and Telecommunications, 2 Chongwen Road, Chongqing 400065, China.
Email: xianggt@cqupt.edu.cn

Xiaojun Wang, Department of Physics & Astronomy, Georgia Southern University, Statesboro, GA 30460, USA.
Email: xwang@georgiasouthern.edu

Jiahua Zhang, State Key Laboratory of Luminescence and Applications, Changchun Institute of Optics, Fine Mechanics and Physics, Chinese Academy of Sciences, 3888 Eastern South Lake Road, Changchun 130033, China.
Email: zhangjh@ciomp.ac.cn

Funding information

National Natural Science Foundation of China, Grant/Award Number: 11704054, 12004061 and 12004062; Science and Technology Research Program of Chongqing Municipal Education Commission, Grant/Award Number: KJZD-K201800602 and KJZD-M202000601

Abstract

Design and fabrication of contactless optical thermometer with rapid and accurate performance has become a research hotspot in recent years. Herein, $\text{CaSc}_2\text{O}_4: \text{Yb}^{3+}/\text{Er}^{3+}$ is employed as the intermediary for temperature sensing under the excitation of 980 nm, which is proven to afford an ultra-sensitive and high-resolution optical thermometry in multiple ways based on the fluorescence intensity ratio (*FIR*) technology. The optimal thermal sensing behaviors are realized by the *FIR* of $\text{Er}^{3+}: {}^2\text{H}_{11/2} \rightarrow {}^4\text{I}_{15/2}$ to ${}^4\text{S}_{3/2} \rightarrow {}^4\text{I}_{15/2}$ transition, which has a relative sensitivity of $1184/T^2$ and a minimal resolution of 0.03 K along with a maximal absolute error of 0.96 K. Besides that, the *FIR* between the thermally coupled Stark sublevels of $\text{Er}^{3+}: {}^4\text{F}_{9/2}$ manifold (*FIR_R*) as well as that of $\text{Er}^{3+}: {}^4\text{I}_{13/2}$ manifold (*FIR_N*) can also provide excellent optical thermometry. The relative sensitivity of *FIR_R*-based and *FIR_N*-based optical thermometers are calculated to be $402/T^2$ and $366/T^2$, respectively, with a same minimal resolution of 0.09 K, which possess the potential to be used for biomedicine due to the inherent advantage of their operating wavelengths located in the biological window. The results demonstrate that $\text{CaSc}_2\text{O}_4: \text{Yb}^{3+}/\text{Er}^{3+}$ is a promising candidate for temperature sensing with multipath, high sensitivity, and superior resolution.

KEYWORDS

$\text{CaSc}_2\text{O}_4: \text{Yb}^{3+}/\text{Er}^{3+}$, electronic level, *FIR* technology, optical thermometry, Stark sublevel

1 | INTRODUCTION

Upconversion (UC) luminescence is referred to radiate ultraviolet or visible light through absorbing two or more near-infrared photons with low energy.¹⁻⁴ Benefiting from such a unique optical property, UC materials have attracted much attention for the application of drug delivery, biological imaging, photodynamic therapy, photothermal therapy, three-dimensional display, etc.⁵⁻⁹ In the past few years, UC materials have also been found to own outstanding temperature sensing properties which can afford a contactless thermometry in many special industries, such as coal mining, metal smelting, petrochemicals, biomedicine, and so on.^{10,11} In particular, the fluorescence intensity ratio (*FIR*) between two thermally coupled energy levels of trivalent rare earth ions is considered to be a promising technology to provide fast and accurate optical thermometry, due to its rapid response capability, high spatial resolution, strong anti-jamming ability, etc.¹²⁻¹⁷ Up to date, numerous trivalent rare earth ions are used for ratiometric thermometry, such as Er^{3+} , Ho^{3+} , Tm^{3+} , Nd^{3+} , and Eu^{3+} .¹⁸⁻²⁵ Among these ions, Er^{3+} is the most widely used activator for temperature sensing which has been realized in an enormous variety of materials, due to the excellent thermal coupling between the green emitting levels $^2\text{H}_{11/2}$ and $^4\text{S}_{3/2}$ of Er^{3+} as well as their strong UC intensity under the excitation of 980 nm excitation with the sensitization of Yb^{3+} .^{26,27} Nevertheless, the thermometric sensitivity and resolution as well as the signal to noise ratio (SNR) of Er^{3+} -typed optical thermometer are still need to be improved.

CaSc_2O_4 is an extremely efficient UC host because of its low phonon energy 540 cm^{-1} , which has been demonstrated in a large number of articles. For instance, Li et al. announce that $\text{CaSc}_2\text{O}_4\text{:Yb}^{3+}/\text{Tm}^{3+}$ exhibits 3.5 times stronger $^3\text{H}_4 \rightarrow ^3\text{H}_6$ near infrared (NIR) emission than that of $\text{Y}_2\text{O}_3\text{:Yb}^{3+}/\text{Tm}^{3+}$, resulting from the larger absorption cross section of Yb^{3+} at 980 nm in CaSc_2O_4 matrix.²⁸ Similar conclusion has also been presented in $\text{CaSc}_2\text{O}_4\text{:Yb}^{3+}/\text{Ho}^{3+}$ and $\text{Y}_2\text{O}_3\text{:Yb}^{3+}/\text{Ho}^{3+}$.²⁹ Beyond that, Stefan's group study the energy transfer (ET) mechanisms between Yb^{3+} and Er^{3+} in CaSc_2O_4 ceramic and obtain a maximal UC efficiency of approximately 0.94%.³⁰ Recognizing the statements mentioned above, it can be proposed that CaSc_2O_4 is a promising candidate to achieve excellent temperature sensing behaviors based on the *FIR* technology in virtue of its outstanding UC luminescence (UCL) performance. However, as far as we know, there are seldom papers in the literature concerning the optical thermometry properties of CaSc_2O_4 .

In the present paper, $\text{CaSc}_2\text{O}_4\text{:Yb}^{3+}/\text{Er}^{3+}$ powders are synthesized through a conventional high temperature solid state reaction and verified by XRD data. Strong UC emission can be observed under the excitation of 980 nm wavelength. The ET mechanisms of the $\text{Yb}^{3+}/\text{Er}^{3+}$ codoped system in CaSc_2O_4 are discussed in detail. Furthermore, the thermal sensing behaviors of $\text{CaSc}_2\text{O}_4\text{:Yb}^{3+}/\text{Er}^{3+}$ are realized in multiple ways based on the *FIR* between two thermally coupled

levels of Er^{3+} , including the electronic levels $^2\text{H}_{11/2}/^4\text{S}_{3/2}$ as well as the Stark sublevels of $^4\text{F}_{9/2}$ manifold and $^4\text{I}_{13/2}$ manifold. The optimal relative sensitivity and resolution is calculated to be $1184/\text{T}^2$ and 0.03 K . All the results reveal that $\text{CaSc}_2\text{O}_4\text{:Yb}^{3+}/\text{Er}^{3+}$ is a promising intermediary for non-contact thermometry with multipath, great sensitivity, and excellent resolution.

2 | EXPERIMENTAL PROCEDURE

2.1 | Sample preparation

A conventional high temperature solid state reaction is used to synthesize $\text{CaSc}_2\text{O}_4\text{:y\% Yb}^{3+}/\text{x\% Er}^{3+}$ ($\text{x} = 0, 1, 2, 3, 4, 5$; $\text{y} = 0, 1, 5, 10, 20, 30, 40$) powder. In a typical procedure, stoichiometric CaCO_3 , Sc_2O_3 , Yb_2O_3 , and Er_2O_3 powder are evenly mixed and ground in an agate mortar for 45 minutes. Subsequently, sinter the mixed powders in a box furnace at 1500°C for 4 hours.

2.2 | Characterization

The powder X-ray diffraction (XRD) data of the prepared samples are examined by a Persee XD-2 diffractometer. A FLS1000 spectrometer equipped a 980 nm diode laser as the excitation source is utilized to measure the spectra data.

3 | RESULTS AND DISCUSSION

3.1 | Crystal structure

The XRD patterns are collected to confirm the structure and phase of $\text{CaSc}_2\text{O}_4\text{:y\% Yb}^{3+}/\text{x\% Er}^{3+}$, as presented in Figure 1A,B. All the diffraction peaks existing in the region of 10° – 70° are perfectly matched with the reference data of CaSc_2O_4 (JCPDS 72-1360) following the well-known calcium ferrite structure with a space group $\text{Pnam}(62)$. As desired, no impure diffraction peaks are observed, revealing that Yb^{3+} and Er^{3+} have successfully entered into the CaSc_2O_4 matrix to form a solid solution structure.

3.2 | Luminescence properties

3.2.1 | UCL properties

Under pumping at 980 nm, the UC spectra of $\text{CaSc}_2\text{O}_4\text{:Yb}^{3+}/\text{Er}^{3+}$ as a function of Er^{3+} and Yb^{3+} doping concentration are recorded at room temperature and presented in Figure 2A,B, respectively. Two obvious emission bands, including

FIGURE 1 XRD patterns of (A) CaSc_2O_4 : 10% $\text{Yb}^{3+}/x\% \text{Er}^{3+}$ and (B) CaSc_2O_4 : $y\% \text{Yb}^{3+}/4\% \text{Er}^{3+}$ along with the standard data of CaSc_2O_4 (JCPDS 72-1360) [Color figure can be viewed at wileyonlinelibrary.com]

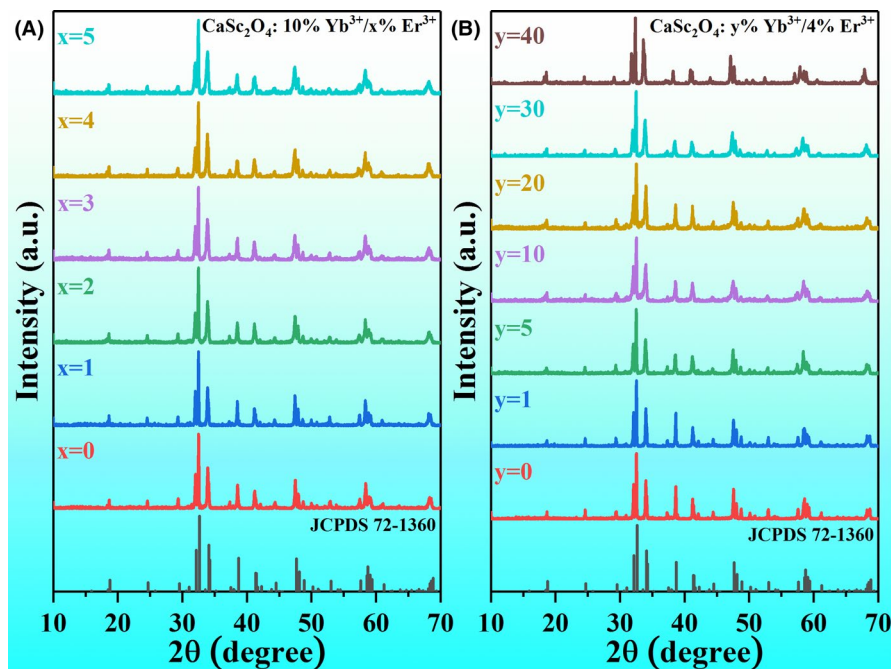
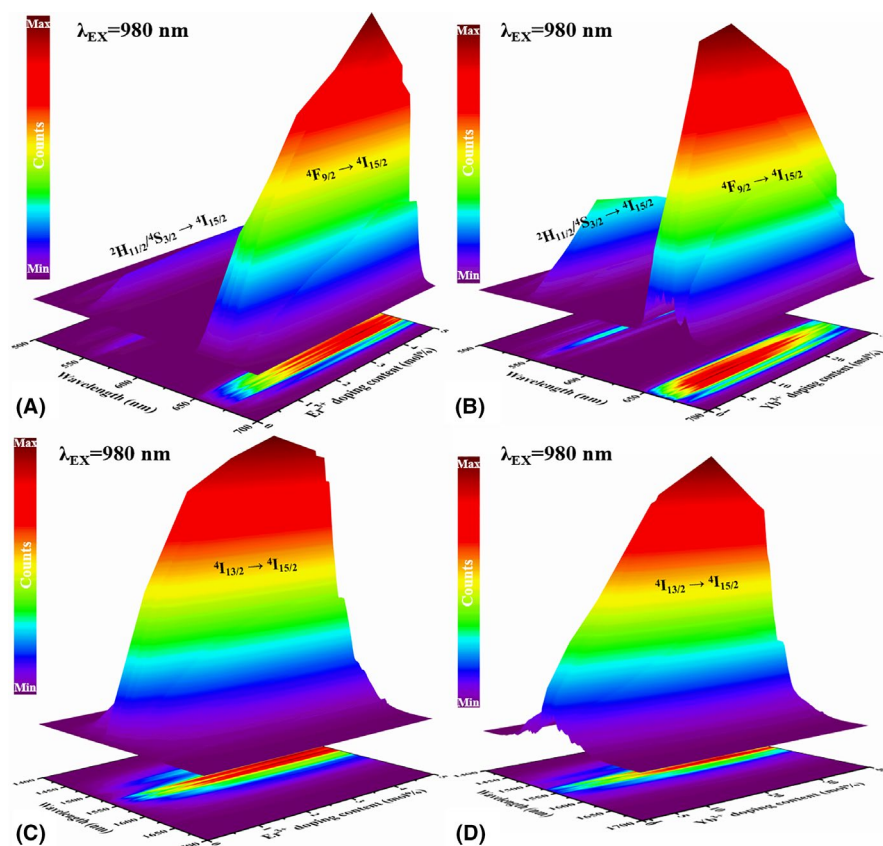


FIGURE 2 UC spectra of (A) CaSc_2O_4 : 10% $\text{Yb}^{3+}/x\% \text{Er}^{3+}$ and (B) CaSc_2O_4 : $y\% \text{Yb}^{3+}/4\% \text{Er}^{3+}$. The NIR spectra of (C) CaSc_2O_4 : 10% $\text{Yb}^{3+}/x\% \text{Er}^{3+}$ and (D) CaSc_2O_4 : $y\% \text{Yb}^{3+}/4\% \text{Er}^{3+}$ [Color figure can be viewed at wileyonlinelibrary.com]



a green one and a red one, appear in the region from 500 nm to 700 nm simultaneously. The green emission band is consisted by two electronic transition of Er^{3+} , which belongs to $^2\text{H}_{11/2} \rightarrow ^4\text{I}_{15/2}$ transition located at 525 nm and $^4\text{S}_{3/2} \rightarrow ^4\text{I}_{15/2}$ transition located at 553 nm. The red one is originated from Er^{3+} : $^4\text{F}_{9/2} \rightarrow ^4\text{I}_{15/2}$ transition peaked at 665 nm. Although the

variation of Er^{3+} and Yb^{3+} doping concentration has no effect on the peak positions, the UC intensities of the presented samples are greatly influenced by the increasing doping concentration of Er^{3+} and Yb^{3+} . Summarizing from Figure 2A,B, the optimal doping concentration of Er^{3+} and Yb^{3+} in CaSc_2O_4 host is ascertained to be 4% and 10%, respectively.

Further increasing the doping concentration of Er^{3+} and Yb^{3+} would give rise to the decrease of UC intensity because of the concentration quenching effect. As for the sample CaSc_2O_4 : 10% Yb^{3+} /4% Er^{3+} , its red UC intensity is about 13.5 times stronger than the green one, mainly caused by the closer $\text{Yb}^{3+}\text{-Er}^{3+}$ and $\text{Er}^{3+}\text{-Er}^{3+}$ pairs created by the substitution of Ca^{2+} and Sc^{3+} .³¹ Actually, a cross relaxation (CR) process exists between Yb^{3+} and Er^{3+} , including $^4\text{S}_{3/2}(\text{Er}^{3+}) + 2\text{F}_{7/2}(\text{Yb}^{3+}) \rightarrow 4\text{I}_{13/2}(\text{Er}^{3+}) + 2\text{F}_{5/2}(\text{Yb}^{3+})$ (CR1) followed by $^4\text{I}_{13/2}(\text{Er}^{3+}) + 2\text{F}_{5/2}(\text{Yb}^{3+}) \rightarrow 4\text{F}_{9/2}(\text{Er}^{3+}) + 2\text{F}_{7/2}(\text{Yb}^{3+})$ (CR2) occurring in the same $\text{Yb}^{3+}\text{-Er}^{3+}$ pair, as shown in Figure 3A. Meanwhile, there is a CR3 process occurring between two Er^{3+} ions, namely $^4\text{F}_{7/2}(\text{Er}^{3+}) + 4\text{I}_{11/2}(\text{Er}^{3+}) \rightarrow 4\text{F}_{9/2}(\text{Er}^{3+}) + 4\text{F}_{9/2}(\text{Er}^{3+})$. The CR processes mentioned above are significantly enhanced by the closer $\text{Yb}^{3+}\text{-Er}^{3+}$ and $\text{Er}^{3+}\text{-Er}^{3+}$ pairs, resulting in an intense red UC emission along with a weak green UC emission.^{32,33} Beyond that, the NIR emission of Er^{3+} attributed to $^4\text{I}_{13/2} \rightarrow ^4\text{I}_{15/2}$ transition is also explored. As depicted in Figure 2C,D, the optimal doping concentration of Er^{3+} and Yb^{3+} in this case is determined to be 4% and 30%, respectively. That is to say, a much higher Yb^{3+} doping concentration is allowed for Er^{3+} : $^4\text{I}_{13/2} \rightarrow ^4\text{I}_{15/2}$ transition, benefiting to achieve strong NIR emission through absorbing more 980 nm photons.³⁴

For the purpose of well understanding the UC mechanism, the power density dependent green and red UC intensities are measured under the excitation of 980 nm wavelength. It is widely known that UCL is assigned to be a complex nonlinear process. However, for the unsaturated UC process, the relationship between the UC intensity I and the excitation power density P can be represented as follows:

$$I \propto P^n. \quad (1)$$

Here n represents the required number of photons for populating the activators from the ground state to the corresponding excited level, which can be acquired through the double

logarithmic plots of the UCL intensity versus the power density.^{35,36} As depicted in Figure 3B, the n values of green and red UCL are both calculated to be approximately 2.0, revealing a two photon process for them in CaSc_2O_4 : $\text{Yb}^{3+}/\text{Er}^{3+}$.

The UC emission of Er^{3+} strongly depends on the ET processes between Yb^{3+} and Er^{3+} . As such, the energy level diagram of Yb^{3+} and Er^{3+} is depicted to illustrate the possible UC mechanisms of $\text{Yb}^{3+}/\text{Er}^{3+}$ codoped system in CaSc_2O_4 . As shown in Figure 3A, upon the excitation of 980 nm wavelength, the laser photons are dominantly absorbed by Yb^{3+} because of its large absorption cross section at this position, giving rise to the population of Yb^{3+} : $^2\text{F}_{5/2}$ state. Subsequently, the Er^{3+} at the ground state is populated to its $^4\text{F}_{7/2}$ state through receiving two 980 nm photons from the excited Yb^{3+} (ET1 and ET2). Then, the green emission from Er^{3+} : $^2\text{H}_{11/2}/^4\text{S}_{3/2}$ states is realized by a multiphonon relaxation (MPR) process originating from $^4\text{F}_{7/2}$ level. The red emitting level Er^{3+} : $^4\text{F}_{9/2}$ is contributed by a MPR process from $^4\text{I}_{11/2}$ level to $^4\text{I}_{13/2}$ level followed by an ET process from Yb^{3+} : $^2\text{F}_{5/2}$ level to Er^{3+} : $^4\text{I}_{13/2}$ level (ET3). In addition, the Er^{3+} located at $^2\text{H}_{11/2}/^4\text{S}_{3/2}$ levels can also undergo a MPR process and then accomplish the population of $^4\text{F}_{9/2}$ level.

3.2.2 | Temperature sensing properties

Figure 4A shows the green UC spectra of CaSc_2O_4 : 10% Yb^{3+} /4% Er^{3+} with the temperature increased from 323 K to 573 K, which are normalized to 1 at 553 nm. There is no obvious shift for the position of green emission band. However, the relative intensity of $^2\text{H}_{11/2} \rightarrow ^4\text{I}_{15/2}$ transition (525 nm) to $^4\text{S}_{3/2} \rightarrow ^4\text{I}_{15/2}$ transition (553 nm) is monotonically increased from ~0.20 to ~0.98 with the rising temperature, as shown in Figure 4B. This can be explained by the thermal population of $^2\text{H}_{11/2}$ state originating from $^4\text{S}_{3/2}$ state due to their moderate energy gap ΔE . That is to say, $^2\text{H}_{11/2}$ and $^4\text{S}_{3/2}$ state are a

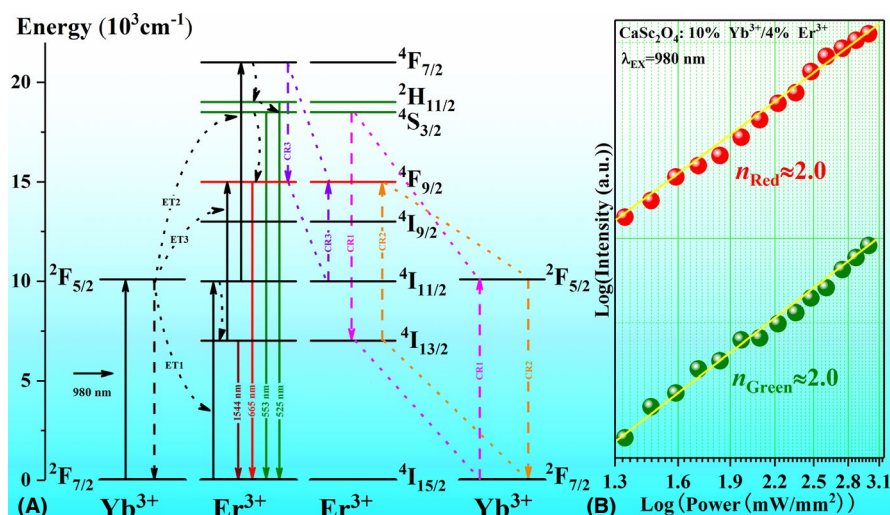


FIGURE 3 (A) Possible ET processes in CaSc_2O_4 : $\text{Yb}^{3+}/\text{Er}^{3+}$. (B) Pump power density dependence of $^2\text{H}_{11/2}/^4\text{S}_{3/2} \rightarrow ^4\text{I}_{15/2}$ transition and $^4\text{F}_{9/2} \rightarrow ^4\text{I}_{15/2}$ transition [Color figure can be viewed at wileyonlinelibrary.com]

pair of thermally coupled energy levels (TCLs) obeying the Boltzmann distribution law:

$$FIR = I_{up}/I_{low} = B \cdot \exp(-\Delta E/k_B T), \quad (2)$$

where I_{up} and I_{low} represent the emission intensity of the upper and lower levels, respectively. k_B is the Boltzmann constant and T is the absolute temperature. B is a constant determined by the degeneracy degree, spontaneous emission, and absorption rate. In the present case, ${}^2H_{11/2}$ and ${}^4S_{3/2}$ are regarded as the upper and lower levels, respectively. According to Eqn (2) and the spectral data, the fitting function of the FIR_G between ${}^2H_{11/2} \rightarrow {}^4I_{15/2}$ transition and ${}^4S_{3/2} \rightarrow {}^4I_{15/2}$ transition is calculated to be

$$FIR_G = 7.7 \cdot e^{-\frac{1184}{T}}, \quad (3)$$

from which the ΔE value is assured to be 824 cm^{-1} , close to the theoretical value 800 cm^{-1} . The experimental data is well fitted with fitting degree (R^2) of 0.9998.

Absolute sensitivity S_A of the FIR -based optical thermometer is the changing rate of FIR values with temperature and relative sensitivity S_R represents the relative change of FIR values per degree of temperature fluctuation. Both of them are the key characteristics for optical thermometers, which can be defined as follows:

$$S_A = |d(FIR)/dT| = FIR \cdot (\Delta E/k_B T^2), \quad (4)$$

$$S_R = |d(FIR)/(FIR) \cdot dT| = \Delta E/k_B T^2. \quad (5)$$

Figure 4C shows the evolution of S_{A-G} and S_{R-G} with the increasing temperature. The S_{A-G} of FIR_G -based optical

thermometer is increased from $0.22\% \text{ K}^{-1}$ to $0.35\% \text{ K}^{-1}$ with the rising temperature. The S_{R-G} is expressed as $1184/T^2$, which is decreased gradually with the temperature increasing from 323 K to 573 K and reaches its maximal value $1.13\% \text{ K}^{-1}$ at 323 K. In addition, the temperature uncertainty δT , namely temperature resolution, is another vital parameter for temperature sensing, which can be calculated by

$$\delta T = (\delta FIR/FIR) \cdot (1/S_R). \quad (6)$$

Here $\delta FIR/FIR$ is the relative uncertainty of FIR , mainly related to the test equipments. Specific to our case, the $\delta FIR/FIR$ value is calculated to be 0.033% for the setup we used in spectrum experiment.³⁷ Figure 4D presents the determined δT_G of FIR_G -based optical thermometer as a function of temperature. Definitely, δT_G is estimated to be better than 0.1 K over the studied temperature region and possesses a minimal value of 0.03 K at 323 K.

With the exception of the electronic energy levels, the Stark sublevels originating from the crystal field effect can also be utilized for temperature sensing due to their thermal coupling derived from the small ΔE . As presented in Figure 5A, the red UC spectra of $\text{CaSc}_2\text{O}_4: 10\% \text{ Yb}^{3+}/4\% \text{ Er}^{3+}$ with various temperature are normalized at 665 nm. More importantly, at least five Stark transitions appear in the red emission band and their relative intensities change regularly with the increasing temperature, indicating their potential for FIR -based optical thermometry. Here, Peak R1 at 652 nm and Peak R2 at 665 nm are selected as the intermediaries for temperature sensing. As shown in Figure 5C, based on the Boltzmann distribution law expressed by Eqn (2), the fitting function of temperature dependent FIR_R between Peak R1 and Peak R2 is determined to be as follows:

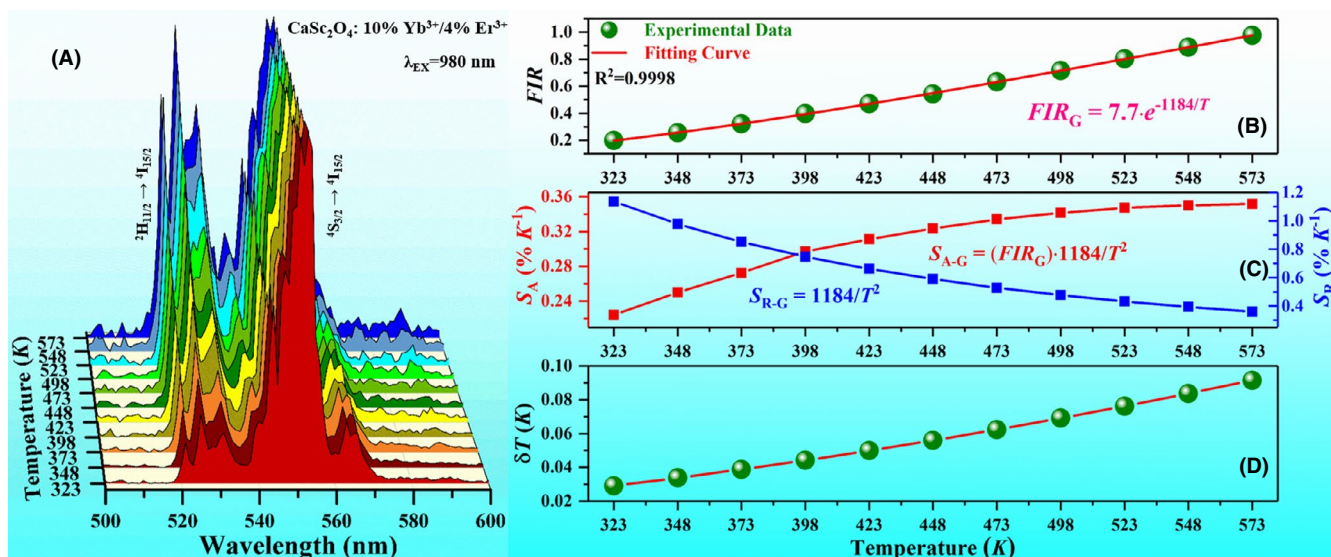


FIGURE 4 (A) Normalized green UC spectra as a function of temperature. The evolution of (B) FIR_G , (C) absolute sensitivity S_{A-G} and relative sensitivity S_{R-G} and (D) temperature resolution δT_G with temperature [Color figure can be viewed at wileyonlinelibrary.com]

$$FIR_R = 1.7e^{-\frac{402}{T}} \quad (7)$$

Correspondingly, the ΔE value between Peak R1 and Peak R2 is calculated to be 280 cm^{-1} , close to the result obtained from the spectra (300 cm^{-1}). In addition, the S_{A-R} and S_{R-R} as well as δT_R of FIR_R -based optical thermometer are all acquired, as depicted in Figure 5D,E. Both S_{A-R} and S_{R-R} reach the maximal value of $0.19\% \text{ K}^{-1}$ and $0.39\% \text{ K}^{-1}$ at the beginning temperature and then decrease gradually with the increasing temperature. The minimal δT_R of FIR_R -based optical thermometer is 0.09 K at the temperature of 323 K . For the $^4I_{13/2} \rightarrow ^4I_{15/2}$ transition in the NIR region, as shown in Figure 5B, thermally coupled Stark transitions located at 1488 nm (Peak N1) and 1544 nm (Peak N2) are chosen as the research subjects for temperature sensing. Figure 5F-H show the corresponding temperature dependence of FIR_N , S_{A-N} , S_{R-N} and δT_N . Consequently, the FIR_N -based optical thermometer owns maximal S_{A-N} and S_{R-N} of about 0.07%

K^{-1} and $0.35\% \text{ K}^{-1}$ as well as a minimal δT_N of 0.09 K at the beginning temperature.

A simple validation experiment is conducted to verify the thermometric accuracy of FIR_G -based and FIR_R -based optical thermometers. A heating gun is used to heat the sample to a certain temperature and then an infrared thermometer is employed to detect the sample temperature. Meanwhile, the green and red UC spectra are collected by the spectrometer excited by 980 nm wavelength. Then the spectral data are utilized to calculate their corresponding temperature based on FIR_G and FIR_R , respectively. As illustrated in Figure 6A,B, both FIR_G -based and FIR_R -based optical thermometers display superior accuracy for optical thermometry. The maximal absolute errors of FIR_G -based and FIR_R -based optical thermometers are 0.96 K and 1.21 K , respectively. In addition, the repeatability studies of FIR_G , FIR_R , and FIR_N in the temperature cycling between 323 K and 573 K have been provided in Figure 7. All of them keep almost unchanged in the cycling process, indicating the excellent repeatability and reliability of $\text{CaSc}_2\text{O}_4: \text{Yb}^{3+}/\text{Er}^{3+}$.

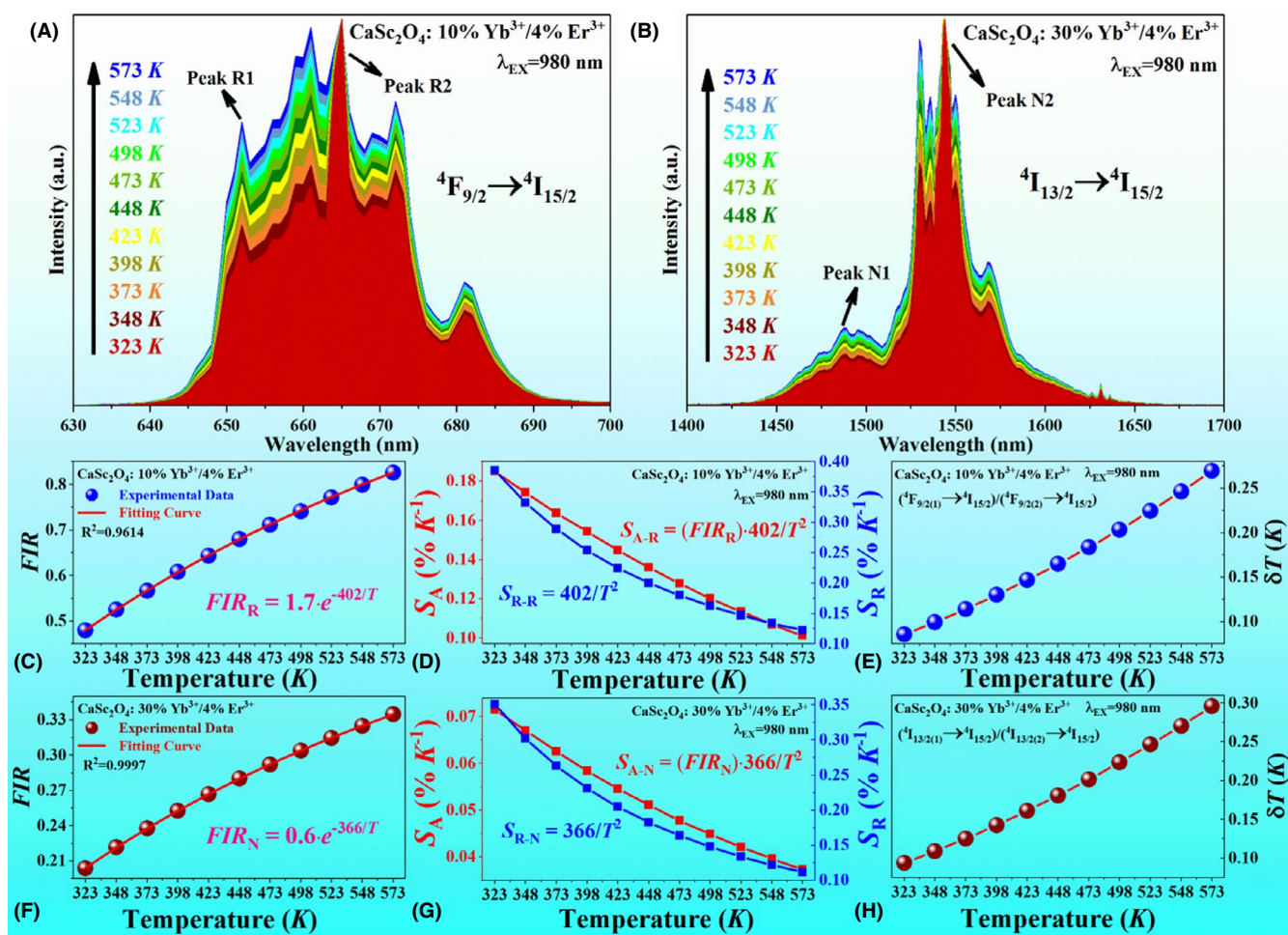


FIGURE 5 Evolution of normalized (A) red UC spectra in $\text{CaSc}_2\text{O}_4: 10\% \text{Yb}^{3+}/4\% \text{Er}^{3+}$ and (B) NIR spectra in $\text{CaSc}_2\text{O}_4: 30\% \text{Yb}^{3+}/4\% \text{Er}^{3+}$ with temperature. The (C) FIR_R , (D) S_{A-R} and S_{R-R} and (e) δT_R of FIR_R -based optical thermometer as a function of temperature. The (F) FIR_N , (G) S_{A-N} and S_{R-N} and (H) δT_N of FIR_N -based optical thermometer as a function of temperature [Color figure can be viewed at wileyonlinelibrary.com]

FIGURE 6 Sample temperature obtained by FIR_G , FIR_R and infrared thermometer along with the corresponding absolute error. Insets are the normalized UC spectra collected at 298 K and 423 K, respectively [Color figure can be viewed at wileyonlinelibrary.com]

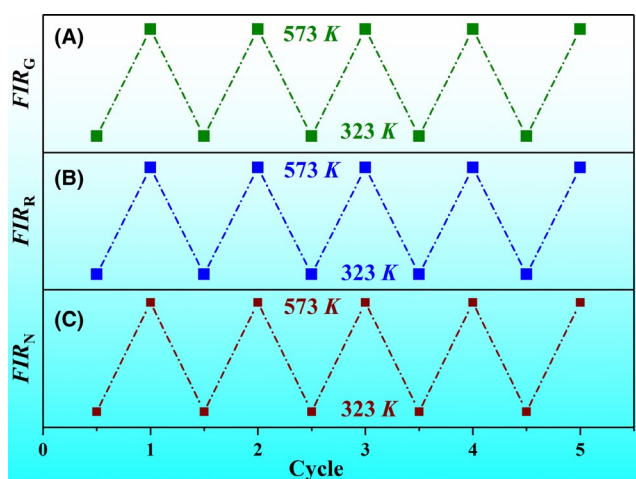
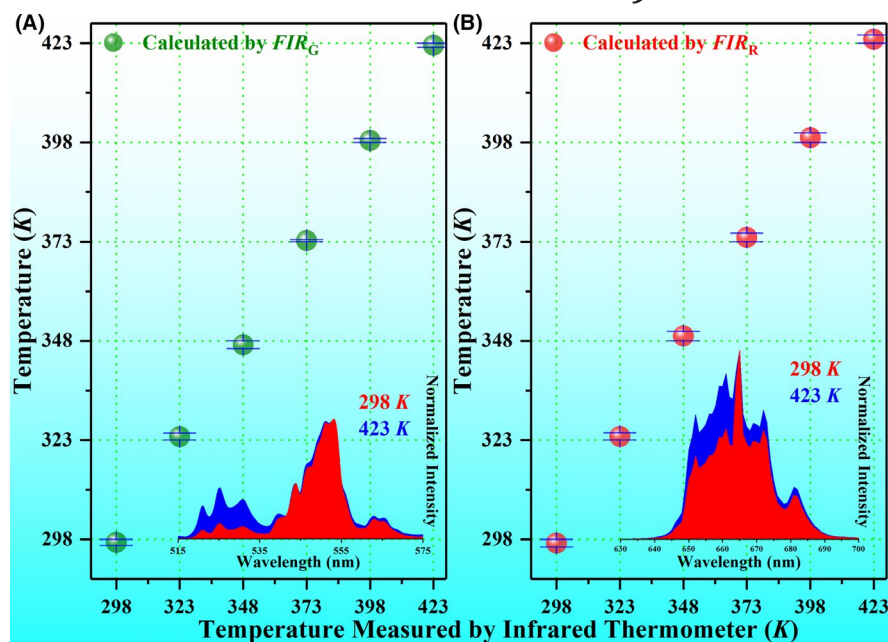


FIGURE 7 The repeatability studies of FIR_G , FIR_R and FIR_N from 323 K to 573 K [Color figure can be viewed at wileyonlinelibrary.com]

Table 1 lists a series of typical FIR -based optical thermometers with their various important parameters. Obviously, as shown in Part A of Table 1, the FIR_G -based optical thermometer realized in $\text{CaSc}_2\text{O}_4:\text{Yb}^{3+}/\text{Er}^{3+}$ shows much larger S_R and lower δT than most others. Although $\text{LaPO}_4:\text{Yb}^{3+}/\text{Nd}^{3+}$ reveals a better temperature sensing performance than the FIR_G -based optical thermometer, the big energy gap between $\text{Nd}^{3+}:$ ${}^4F_{7/2}$ and ${}^4F_{3/2}$ (1897 cm^{-1}) makes it more suitable for high-temperature detection resulting from the requirement of strong heat activation for the lower level to populate the upper level. Meanwhile, as shown in Part B of Table 1, the FIR_R -based and FIR_N -based optical thermometers in this work also exhibit remarkable

temperature sensing behaviors among the optical thermometers based on the thermally coupled Stark sublevels. By the way, although the FIR_G -based optical thermometer owns much better thermometric performance than that of the FIR_R -based and FIR_N -based optical thermometers, the FIR_R -based and FIR_N -based optical thermometers possess potential application values for biomedicine thanks to the proper wavelengths employed for optical thermometry, which exactly locate in the biological window. All the results indicate that $\text{CaSc}_2\text{O}_4:\text{Yb}^{3+}/\text{Er}^{3+}$ is a promising candidate for temperature sensing with multipath, high sensitivity and superior resolution.

4 | CONCLUSIONS

In summary, multipath FIR -based optical thermometry is successfully realized in $\text{CaSc}_2\text{O}_4:\text{Yb}^{3+}/\text{Er}^{3+}$ based on the thermally coupled electronic levels ${}^2H_{11/2}/{}^4S_{3/2}$ (FIR_G), Stark sublevels of ${}^4F_{9/2}$ manifold (FIR_R) and ${}^4I_{13/2}$ manifold (FIR_N), respectively. Thereinto, FIR_G -based optical thermometer owns the optimal temperature sensing behaviors with a S_{R-G} of $1184/T^2$ and a minimal resolution of 0.03 K as well as a maximal absolute error of 0.96 K . The S_R of FIR_R -based and FIR_N -based optical thermometers are calculated to be $402/T^2$ and $366/T^2$ respectively with a same minimal resolution of 0.09 K , which can be utilized for biomedicine due to the advantage of their operating wavelengths located in the biological window. The great sensitivity and ultra-high resolution demonstrate the tremendous potential of $\text{CaSc}_2\text{O}_4:\text{Yb}^{3+}/\text{Er}^{3+}$ to be an optical thermometer with multipath.

TABLE 1 Important parameters of several typical FIR-based optical thermometers

Host	Dopants	Transition	Wavelength (nm)	Working Range (K)	S_R (%K ⁻¹)	δT_{\min} (K)	Reference
Part A: Optical thermometers based on electronic levels							
CaSc ₂ O ₄	Yb ³⁺ /Er ³⁺	Er ³⁺ : (² H _{11/2} → ⁴ I _{15/2})/(⁴ S _{3/2} → ⁴ I _{15/2})	525/553	323–573	1184/T ²	0.03	This work
NaY(WO ₄) ₂	Yb ³⁺ /Er ³⁺	Er ³⁺ : (² H _{11/2} → ⁴ I _{15/2})/(⁴ S _{3/2} → ⁴ I _{15/2})	530/552	293–503	1127/T ²	0.4	38
NaYF ₄	Yb ³⁺ /Er ³⁺	Er ³⁺ : (² H _{11/2} → ⁴ I _{15/2})/(⁴ S _{3/2} → ⁴ I _{15/2})	521/540	258–423	1123/T ²	0.1	39
CaMoO ₄	Yb ³⁺ /Er ³⁺ /Na ⁺ /K ⁺	Er ³⁺ : (² H _{11/2} → ⁴ I _{15/2})/(⁴ S _{3/2} → ⁴ I _{15/2})	530/552	306–513	1193/T ²	—	40
CaMoO ₄	Yb ³⁺ /Er ³⁺	Er ³⁺ : (² H _{11/2} → ⁴ I _{15/2})/(⁴ S _{3/2} → ⁴ I _{15/2})	530/552	300–760	1072/T ²	—	41
YVO ₄	Yb ³⁺ /Er ³⁺	Er ³⁺ : (² H _{11/2} → ⁴ I _{15/2})/(⁴ S _{3/2} → ⁴ I _{15/2})	524/554	302–483	774/T ²	—	42
La ₂ (MoO ₄) ₃	Yb ³⁺ /Er ³⁺	Er ³⁺ : (² H _{11/2} → ⁴ I _{15/2})/(⁴ S _{3/2} → ⁴ I _{15/2})	525/548	300–500	670/T ²	—	43
CaWO ₄	Yb ³⁺ /Er ³⁺	Er ³⁺ : (⁴ F _{7/2} → ⁴ I _{15/2})/(⁴ S _{3/2} → ⁴ I _{15/2})	490/551	693–813	2820/T ²	1.02	44
La ₂ O ₃	Yb ³⁺ /Nd ³⁺	Nd ³⁺ : (⁴ F _{7/2} → ⁴ I _{9/2})/(⁴ F _{5/2} → ⁴ I _{9/2})	765/825	293–1233	1334/T ²	0.1	45
LaPO ₄	Yb ³⁺ /Nd ³⁺	Nd ³⁺ : (⁴ F _{7/2} → ⁴ I _{9/2})/(⁴ F _{3/2} → ⁴ I _{9/2})	749/864	280–490	2727/T ²	0.02	46
Part B: Optical thermometers based on Stark sublevels							
CaSc ₂ O ₄	Yb ³⁺ /Er ³⁺	Er ³⁺ : ⁴ F _{9/2} → ⁴ I _{15/2}	652/665	323–573	402/T ²	0.09	This work
CaSc ₂ O ₄	Yb ³⁺ /Er ³⁺	Er ³⁺ : ⁴ I _{13/2} → ⁴ I _{15/2}	1488/1544	323–573	366/T ²	0.09	This work
Ba ₅ Gd ₈ Zn ₄ O ₂₁	Yb ³⁺ /Er ³⁺	Er ³⁺ : ⁴ F _{9/2} → ⁴ I _{15/2}	653/674	200–490	144/T ²	—	32
Ba ₃ Y ₄ O ₉	Yb ³⁺ /Er ³⁺	Er ³⁺ : ⁴ F _{9/2} → ⁴ I _{15/2}	656/664	83–563	270/T ²	—	47
BaMoO ₄	Yb ³⁺ /Er ³⁺	Er ³⁺ : ⁴ I _{13/2} → ⁴ I _{15/2}	1521/1531	293–553	110/T ²	—	48
CaO-Y ₂ O ₃	Yb ³⁺ /Er ³⁺	Er ³⁺ : ⁴ I _{13/2} → ⁴ I _{15/2}	1476/1534	303–573	405/T ²	—	49
NaYbF ₄	Tm ³⁺	Tm ³⁺ : ³ H ₄ → ³ H ₆	801/820	10–295	190/T ²	—	50
YVO ₄	Nd ³⁺	Nd ³⁺ : ⁴ F _{3/2} → ⁴ I _{11/2}	1063/1071	298–333	186/T ²	1.5	51

ACKNOWLEDGEMENTS

This work is financially supported by National Natural Science Foundation of China (11704054, 12004061, 12004062) and Science and Technology Research Program of Chongqing Municipal Education Commission (KJZD-K201800602, KJZD-M202000601).

ORCID

Guotao Xiang  <https://orcid.org/0000-0003-3587-6654>

Sha Jiang  <https://orcid.org/0000-0001-7336-2115>

Xianju Zhou  <https://orcid.org/0000-0003-0708-6081>

Li Li  <https://orcid.org/0000-0003-1163-5733>

REFERENCES

- Auzel F. Upconversion and anti-stokes processes with f and d ions in solids. *Chem Rev.* 2004;104:139–74.
- Zhang JH, Hao ZD, Li J, Zhang X, Luo YS, Pan GH. Observation of efficient population of the red-emitting state from the green state by non-multiphonon relaxation in the Er³⁺-Yb³⁺ system. *Light Sci Appl.* 2015;4:e239.
- Wang F, Wen SH, He H, Wang BM, Zhou ZG, Shimoni O, et al. Microscopic inspection and tracking of single upconversion nanoparticles in living cells. *Light Sci Appl.* 2018;7:18007.
- Liu KC, Zhang ZY, Shan CX, Feng ZQ, Li JS, Song CL, et al. A flexible and superhydrophobic upconversion-luminescence membrane as an ultrasensitive fluorescence sensor for single droplet detection. *Light Sci Appl.* 2016;5:e16136.
- Zhang Z, Jayakumar MKG, Shikha S, Zhang Y, Zheng X, Zhang Y. Modularly assembled upconversion nanoparticles for orthogonally controlled cell imaging and drug delivery. *ACS Appl Mater Inter.* 2020;12:12549–56.
- Liu YW, Teitelboim A, Fernandez-Bravo A, Yao KY, Altoe MVP, Aloni S, et al. Controlled assembly of upconverting nanoparticles for low-threshold microlasers and their imaging in scattering media. *ACS Nano.* 2020;14:1508–19.
- Li YY, Zhang XB, Zhang Y, Zhang Y, He YL, Liu Y, et al. Activatable photodynamic therapy with therapeutic effect prediction based on a self-correction upconversion nanoprobe. *ACS Appl Mater Inter.* 2020;12:19313–23.
- Qiu XC, Zhou QW, Zhu XJ, Wu ZG, Feng W, Li FY. Ratiometric upconversion nanothermometry with dual emission at the same wavelength decoded via a time-resolved technique. *Nat Commun.* 2020;11:4.
- Gao LX, Shan XC, Xu XX, Liu YT, Liu BL, Li SQ, et al. Video-rate upconversion display from optimized lanthanide ion doped upconversion nanoparticles. *Nanoscale.* 2020;12:18987.
- Goderski S, Runowski M, Wozny P, Lavin V, Lis S. Lanthanide upconverted luminescence for simultaneous contactless optical thermometry and manometry-sensing under extreme conditions of pressure and temperature. *ACS Appl Mater Inter.* 2020;12:40475–85.
- Casagrande E, Back M, Cristofori D, Ueda J, Tanabe S, Palazzolo S, et al. Upconversion-mediated Boltzmann thermometry in double-layered Bi₂SiO₅:Yb³⁺, Tm³⁺@SiO₂ hollow nanoparticles. *J Mater Chem C.* 2020;8:7828–36.
- Xiang GT, Liu XT, Zhang JH, Liu Z, Liu W, Ma Y, et al. Dual-mode optical thermometry based on the fluorescence intensity

- ratio excited by a 915 nm wavelength in $\text{LuVO}_4:\text{Yb}^{3+}/\text{Er}^{3+}@\text{SiO}_2$ nanoparticles. *Inorg Chem.* 2019;58:8245–52.
13. Ma Y, Xiang GT, Zhang JH, Liu Z, Zhou P, Liu W, et al. Upconversion properties and temperature sensing behaviors in visible and near-infrared region based on fluorescence intensity ratio in $\text{LuVO}_4:\text{Yb}^{3+}/\text{Er}^{3+}$. *J Alloy Compd.* 2018;769:325–31.
 14. Cao BS, Bao YA, Liu Y, Shang JY, Zhang ZY, He YY, et al. Wide-range and highly-sensitive optical thermometers based on the temperature-dependent energy transfer from Er to Nd in Er/Yb/Nd codoped NaYF_4 upconversion nanocrystals. *Chem Eng J.* 2020;385:123906.
 15. Jiang YC, Tong Y, Chen SYZ, Zhang WN, Hu FF, Wei RF, et al. A three-mode self-referenced optical thermometry based on up-conversion luminescence of $\text{Ca}_2\text{MgWO}_6:\text{Er}^{3+}, \text{Yb}^{3+}$ phosphors. *Chem Eng J.* 2020; <https://doi.org/10.1016/j.cej.2020.127470>.
 16. Xie CY, Zhao L, Jiang B, Mao JS, Lin Y, Wang P, et al. Dual-activator luminescence of $\text{LuAG}:\text{Mn}^{4+}/\text{Tb}^{3+}$ phosphor for optical thermometry. *J Am Ceram Soc.* 2019;102:7500–8.
 17. Li XM, Cao JK, Wei YL, Yang ZR, Guo H. Optical thermometry based on up-conversion luminescence behavior of Er^{3+} -doped transparent Sr_2YbF_7 glass-ceramics. *J Am Ceram Soc.* 2015;98:3824–30.
 18. Ge WY, Xu MM, Shi JD, Zhu JF, Li YX. Highly temperature-sensitive and blue upconversion luminescence properties of $\text{Bi}_2\text{Ti}_2\text{O}_7:\text{Tm}^{3+}/\text{Yb}^{3+}$ nanofibers by electrospinning. *Chem Eng J.* 2020;391:123546.
 19. Liu GF, Sun Z, Fu ZL, Ma L, Wang XJ. Temperature sensing and bio-imaging applications based on polyethylenimine/ CaF_2 nanoparticles with upconversion fluorescence. *Talanta.* 2017;169:181–8.
 20. Chai XN, Li J, Wang XS, Li YX, Yao X. Upconversion luminescence and temperature-sensing properties of $\text{Ho}^{3+}/\text{Yb}^{3+}$ -codoped ZnWO_4 phosphors based on fluorescence intensity ratios. *RSC Adv.* 2017;7:40046–52.
 21. Xu W, Zhao H, Zhang ZG, Cao WW. Highly sensitive optical thermometry through thermally enhanced near infrared emissions from $\text{Nd}^{3+}/\text{Yb}^{3+}$ codoped oxyfluoride glass ceramic. *Sensor Actuat B: Chem.* 2013;178:520–4.
 22. Li L, Tang XH, Wu ZJ, Zheng YF, Jiang S, Tang X, et al. Simultaneously tuning emission color and realizing optical thermometry via efficient $\text{Tb}^{3+} \rightarrow \text{Eu}^{3+}$ energy transfer in whitlockite-type phosphate multifunctional phosphors. *J Alloy Compd.* 2019;780:266–75.
 23. Zhang J, Cai GM, Wang WJ, Ma L, Wang XJ, Jin ZP. Tuning of emission by Eu^{3+} concentration in a pyrophosphate: the effect of local symmetry. *Inorg Chem.* 2020;59:2241–7.
 24. Li GH, Yang N, Guo JG, Wang ZL, Cai GM, Wang XJ. Efficient and stable $\text{Sr}_3\text{Eu}_2\text{B}_4\text{O}_{12}$ red phosphor benefiting from low symmetry and distorted local environment. *Dalton Trans.* 2020;49:3260–71.
 25. Wu ZC, Cui LL, Zhang X, Zhang XX, Liu J, Ma L, et al. Cationic substitution induced tuning of photoluminescence in $\text{Ba}_{2.94-2x}\text{La}_x\text{Na}_x\text{P}_4\text{O}_{13}:0.06\text{Eu}$ phosphors for WLEDs. *J Alloy Compd.* 2020;835(155109).
 26. Xiang GT, Xia Q, Liu XT, Wang XJ. Optical thermometry based on the thermally coupled energy levels of Er^{3+} in upconversion materials. *Dalton Trans.* 2020;49:17115–20.
 27. Xiang GT, Liu XT, Xia Q, Jiang S, Zhou XJ, Li L, et al. Deep-tissue temperature sensing realized in $\text{BaY}_2\text{O}_4:\text{Yb}^{3+}/\text{Er}^{3+}$ with ultrahigh sensitivity and extremely intense red upconversion luminescence. *Inorg Chem.* 2020;59:11054–60.
 28. Li J, Zhang JH, Hao ZD, Zhang X, Zhao JH, Luo YS. Intense up-conversion luminescence and origin study in $\text{Tm}^{3+}/\text{Yb}^{3+}$ codoped calcium scandate. *Appl Phys Lett.* 2012;101:121905.
 29. Li J, Zhang JH, Hao ZD, Chen L, Zhang X, Luo YS. Intense Upconversion luminescence of $\text{CaSc}_2\text{O}_4:\text{Ho}^{3+}/\text{Yb}^{3+}$ from large absorption cross section and energy-transfer rate of Yb^{3+} . *Chem Phys Chem.* 2015;16:1366–9.
 30. Ștefan A, Toma O, Georgescu Ș. Upconversion luminescence in CaSc_2O_4 doped with Er^{3+} and Yb^{3+} . *J Lumin.* 2016;180:376–83.
 31. Teng X, Zhu YH, Wei W, Wang SC, Huang JF, Naccache R, et al. Lanthanide-doped $\text{Na}_x\text{ScF}_{3+x}$ nanocrystals: crystal structure evolution and multicolor tuning. *J Am Chem Soc.* 2012;134:8340–3.
 32. Suo H, Guo CF, Li T. Broad-scope thermometry based on dual-color modulation up-conversion phosphor $\text{Ba}_3\text{Gd}_8\text{Zn}_4\text{O}_{21}:\text{Er}^{3+}/\text{Yb}^{3+}$. *J Phys Chem C.* 2016;120:2914–24.
 33. Xiang GT, Zhang JH, Hao ZD, Zhang X, Pan GH, Luo YS, et al. Importance of suppression of Yb^{3+} -de-excitation to upconversion enhancement in $\beta\text{-NaYF}_4:\text{Yb}^{3+}/\text{Er}^{3+}@\beta\text{-NaYF}_4$ sandwiched structure nanocrystals. *Inorg Chem.* 2015;54:3921–8.
 34. Wen SH, Zhou JJ, Zheng KZ, Bednarkiewicz A, Liu XG, Jin DY. Advances in highly doped upconversion nanoparticles. *Nat Commun.* 2018;9:2415.
 35. Mahata MK, Koppe T, Mondal T, Brüsewitz C, Kumar K, Rai VK, et al. Incorporation of Zn^{2+} ions into $\text{BaTiO}_3:\text{Er}^{3+}/\text{Yb}^{3+}$ nanophosphor: an effective way to enhance upconversion, defect luminescence and temperature sensing. *Phys Chem Chem Phys.* 2015;17:20741–53.
 36. Sinha S, Mahata MK, Kumar K. Enhancing the upconversion luminescence properties of $\text{Er}^{3+}\text{-Yb}^{3+}$ doped yttrium molybdate through Mg^{2+} incorporation: effect of laser excitation power on temperature sensing and heat generation. *New J Chem.* 2019;43:5960–71.
 37. Zhou X, Wang YJ, Wang HW, Xiang L, Yan YL, Li L, et al. Nd^{3+} and $\text{Nd}^{3+}/\text{Yb}^{3+}$ -incorporated complexes as optical thermometer working in the second biological window. *Sens Biosensing Res.* 2020;29:100345.
 38. Lin M, Xie LJ, Wang ZJ, Richards BS, Gao GJ, Zhong JP. Facile synthesis of mono-disperse sub-20 nm $\text{NaY(WO}_4)_2:\text{Er}^{3+}, \text{Yb}^{3+}$ upconversion nanoparticles: a new choice for nanothermometry. *J Mater Chem C.* 2019;7:2971–7.
 39. Zhang H, Ye JT, Wang XL, Zhao SL, Lei RS, Huang LH, et al. Highly reliable all-fiber temperature sensor based on the fluorescence intensity ratio (FIR) technique in $\text{Er}^{3+}/\text{Yb}^{3+}$ co-doped NaYF_4 phosphors. *J Mater Chem C.* 2019;7:15269–75.
 40. Sinha S, Mahata MK, Swart HC, Kumar A, Kumar K, et al. Enhancement of upconversion, temperature sensing and cathodoluminescence in the K^+/Na^+ compensated $\text{CaMoO}_4:\text{Er}^{3+}/\text{Yb}^{3+}$ nanophosphor. *New J Chem.* 2017;41:5362–72.
 41. Sinha S, Mahata MK, Kumar K, Tiwari SP, Rai VK. Dualistic temperature sensing in $\text{Er}^{3+}/\text{Yb}^{3+}$ doped CaMoO_4 upconversion phosphor. *Spectrochim Acta A.* 2017;173:369–75.
 42. Mahata MK, Kumar K, Rai VK. $\text{Er}^{3+}\text{-Yb}^{3+}$ doped vanadate nanocrystals: a highly sensitive thermographic phosphor and its optical nanoheater behavior. *Sensor Actuat B: Chem.* 2015;209:775–80.
 43. Sinha S, Mahata MK, Kumar K. Comparative thermometric properties of bi-functional $\text{Er}^{3+}\text{-Yb}^{3+}$ doped rare earth ($\text{RE} = \text{Y, Gd and La}$) molybdates. *Mater Res Express.* 2018;5:026201.
 44. Li LP, Qin F, Zheng YD, Zhang ZG. Strategy for highly sensitive optical ratiometric temperature measurement. *Opt Mater Express.* 2019;9:3260–7.
 45. Gao GJ, Busko D, Kauffmann-Weiss S, Turshatov A, Howard IA, Richards BS. Wide-range non-contact fluorescence intensity ratio

- thermometer based on $\text{Yb}^{3+}/\text{Nd}^{3+}$ co-doped La_2O_3 microcrystals operating from 290 to 1230 K. *J Mater Chem C*. 2018;6:4163–70.
46. Suo H, Zhao XQ, Zhang ZY, Guo CF. Ultra-sensitive optical nano-thermometer LaPO_4 : $\text{Yb}^{3+}/\text{Nd}^{3+}$ based on thermo-enhanced NIR-to-NIR emissions. *Chem Eng J*. 2020;389:124506.
 47. Wu H, Hao ZD, Zhang LL, Zhang X, Xiao Y, Pan GH, et al. $\text{Er}^{3+}/\text{Yb}^{3+}$ codoped phosphor $\text{Ba}_3\text{Y}_4\text{O}_9$ with intense red upconversion emission and optical temperature sensing behavior. *J. Mater. Chem. C*. 2018;6:3459–67.
 48. Lei RS, Liu X, Huang FF, Deng DG, Zhao SL, Xu H, et al. Optical thermometry based on anomalous temperature-dependent 1.53 μm infrared luminescence of Er^{3+} in BaMoO_4 : $\text{Er}^{3+}/\text{Yb}^{3+}$ phosphor. *Opt Mater*. 2018;86:278–85.
 49. Xiang GT, Liu XT, Liu W, Wang B, Liu Z, Jiang S, et al. Multifunctional optical thermometry based on the stark sublevels of Er^{3+} in $\text{CaO-Y}_2\text{O}_3$: $\text{Yb}^{3+}/\text{Er}^{3+}$. *J Am Ceram Soc*. 2019;103:2540–7.
 50. Shang YF, Han Q, Hao SW, Chen T, Zhu YY, Wang ZY, et al. Dual-mode upconversion nanoprobe enables broad-range thermometry from cryogenic to room temperature. *ACS Appl Mater Inter*. 2019;11:2455–42461.
 51. Kolesnikov IE, Golyeva EV, Kalinichev AA, Kurochkin MA, Lähderanta E, Mikhailov MD. Nd^{3+} single doped YVO_4 nanoparticles for sub-tissue heating and thermal sensing in the second biological window. *Sensor Actuat B: Chem*. 2017;243:338–45.

How to cite this article: Xiang G, Xia Q, Xu S, et al. Multipath optical thermometry realized in CaSc_2O_4 : $\text{Yb}^{3+}/\text{Er}^{3+}$ with high sensitivity and superior resolution. *J Am Ceram Soc*. 2021;104:2711–2720. <https://doi.org/10.1111/jace.17686>